Atmos. Chem. Phys., 20, 2695–2707, 2020
https://doi.org/10.5194/acp-20-2695-2020
© Author(s) 2020. This work is distributed under
the Creative Commons Attribution 4.0 License.

Atmospheric Chemistry and Physics
Open Access
EGU

Kinetic and mechanistic study of the reaction between methane sulfonamide ($CH_3S(O)_2NH_2$) and OH

Matias Berasategui, Damien Amedro, Achim Edtbauer, Jonathan Williams, Jos Lelieveld, and John N. Crowley

Division of Atmospheric Chemistry, Max-Planck-Institut für Chemie, 55128 Mainz, Germany

Correspondence: John N. Crowley (john.crowley@mpic.de)

Received: 8 November 2019 – Discussion started: 28 November 2019
Revised: 30 January 2020 – Accepted: 3 February 2020 – Published: 4 March 2020

Abstract. Methane sulfonamide (MSAM), $CH_3S(O)_2NH_2$, was recently detected for the first time in ambient air over the Red Sea and the Gulf of Aden where peak mixing ratios of ≈ 60 pptv were recorded. Prior to this study the rate constant for its reaction with the OH radical and the products thereby formed were unknown, precluding assessment of its role in the atmosphere. We have studied the OH-initiated photo-oxidation of MSAM in air (298 K, 700 Torr total pressure) in a photochemical reactor using in situ detection of MSAM and its products by Fourier transform infrared (FTIR) absorption spectroscopy. The relative rate technique, using three different reference compounds, was used to derive a rate coefficient of $(1.4 \pm 0.3) \times 10^{-13}$ cm^3 molec.$^{-1}$ s^{-1}. The main end products of the photo-oxidation observed by FTIR were CO_2, CO, SO_2, and HNO_3 with molar yields of (0.73 ± 0.11), (0.28 ± 0.04), (0.96 ± 0.15), and (0.62 ± 0.09), respectively. N_2O and HC(O)OH were also observed in smaller yields of (0.09 ± 0.02) and (0.03 ± 0.01). Both the low rate coefficient and the products formed are consistent with hydrogen abstraction from the $-CH_3$ group as the dominant initial step. Based on our results MSAM has an atmospheric lifetime with respect to loss by reaction with OH of about 80 d.

1 Introduction

Natural emissions of organosulfur compounds from phytoplankton comprise up to 60 % of the total sulfur flux into the marine boundary layer (Andreae, 1990; Bates et al., 1992; Spiro et al., 1992), and in remote oceanic areas they are the main source of climatically active sulfate aerosols, which can influence the radiation balance at the earth's surface (Charlson et al., 1987; Andreae and Crutzen, 1997). The main organosulfur trace gases in the marine boundary layer are dimethyl sulfide (CH_3SCH_3, DMS) and its oxidation products dimethyl sulfoxide (DMSO), dimethyl sulfone ($DMSO_2$), methyl sulfonic acid (MSA), and methyl sulfinic acid (MSI) for which atmospheric lifetimes with respect to their degradation by the OH radical vary between hours (DMS) and several weeks ($DMSO_2$).

Recently, the first detection of methane sulfonamide ($CH_3S(O)_2NH_2$, MSAM) in ambient air was made during the Air Quality and Climate Change in the Arabian Basin (AQABA-2017) campaign. Mixing ratios of MSAM approached 60 pptv over the Arabian Sea; details of these measurements and a discussion of the likely sources of MSAM in these regions are given in a companion paper (Edtbauer et al., 2019). As MSAM had not been considered to be an atmospheric trace gas prior to the observations of Edtbauer et al. (2019), there have been no laboratory studies to investigate either its spectroscopy or the kinetics of its reactions with atmospheric radicals, such as OH, so that its atmospheric lifetime and the products formed during its degradation in air were unknown. Combining carbon, nitrogen, sulfur, and oxygen in a single, small molecule, MSAM is an intriguing species not only as an atmospheric trace gas but also from a spectroscopic and kinetic perspective. Unlike basic alkyl amines such as, for example, CH_3NH_2, MSAM contains an acidic $-NH_2$ group (Remko, 2003).

This work presents the first kinetic and mechanistic study of the OH-induced oxidation of MSAM in air. A reaction mechanism is proposed that, through numerical simulation, describes the time-dependent formation of the end products we observed. From these results, we calculate the lifetime and the likely role of MSAM in the atmosphere.

2 Methods

2.1 Experimental set-up

The experimental set-up used to study the reaction of OH with MSAM has been described in detail previously (Crowley et al., 1999; Bunkan et al., 2018). Briefly, the reaction vessel was a 44.39 L cylindrical quartz-wall chamber equipped with a White-type multiple-reflection mirror system resulting in an 86.3 m optical path length for absorption spectroscopy in the infrared. The quartz reactor was at room temperature (296 ± 2 K) and for most experiments at 700 Torr total pressure (1 Torr = 1.333 hPa) using synthetic air bath gas. Six external, radially mounted, low-pressure Hg lamps emitting mainly at 253.65 nm provided a homogeneous light flux within the reactor for radical generation. A 1000 Torr capacitance manometer was used to measure the pressure inside the reactor.

MSAM and other gases used to generate OH (see below) were mixed in a glass vacuum line which was connected directly to the reaction chamber by a PTFE piping. Two capacitance manometers (10 and 100 Torr ranges) were used to accurately measure pressures in the vacuum line. Crystalline MSAM melts at 363 K and has a boiling point of approximately 453 K and an unknown vapour pressure (< 0.02 Torr) at room temperature. Owing to its low vapour pressure, MSAM was eluted into the reaction chamber by flowing synthetic air (450 cm^3 STP min^{-1}, sccm) through a finger containing crystalline MSAM warmed to 333 K and subsequently through a cold trap at 298 K (to prevent condensation downstream). This way we could ensure that the saturation vapour pressure of MSAM at 298 K was achieved. In initial experiments without the trap we observed extra absorption features, which could be assigned to a dimer of MSAM (see below).

Gas-phase infrared spectra in the range of 4000–600 cm^{-1} were recorded with a resolution of 2 cm^{-1} from 16 co-added interferograms (128 scans for the background) using a Fourier transform infrared (FTIR) spectrometer (Bruker Vector 22) equipped with an external photoconductive mercury–cadmium–telluride (MCT) detector cooled to liquid nitrogen temperature. OPUS software was used to analyse and manipulate the IR spectra. Interferograms were phase-corrected (Mertz) and Boxcar apodized with a zero-filling factor of 4. Most of the products obtained (CO_2, CO, HC(O)OH, HNO_3, and SO_2) were identified and quantified from the IR reference spectra of pure samples under similar experimental conditions (700 Torr and 298.2 K, Fig. S1 in the Supplement).

The low vapour pressure of MSAM precluded accurate dosing into the chamber and thus generation of a calibration spectrum. In order to calibrate the infrared absorption features of MSAM, we oxidized it in air and then conducted a sulfur and nitrogen balance of the products. As discussed below, the only sulfur-containing product detected from MSAM degradation was SO_2 (which can easily be calibrated), and the only nitrogen-containing products were HNO_3 and N_2O, which can also be calibrated. Experiments in which MSAM was almost completely converted to known amounts of SO_2, HNO_3, and N_2O thus provided an indirect calibration (via assumption of 100 % sulfur or nitrogen balance) of its concentration and thus IR cross sections.

2.2 Generation of OH

OH was generated by the 254 nm photolysis of O_3 in the presence of H_2.

$$O_3 + h\nu(254\,\text{nm}) \rightarrow O(^1D) + O_2 \quad \text{(R1)}$$

$$O(^1D) + H_2 \rightarrow OH + H \quad \text{(R2)}$$

$$H + O_2 + M \rightarrow HO_2 + M \quad \text{(R3)}$$

Further reactions that cycle OH and HO_2 (e.g. $OH + H_2$, $H + O_3$, $HO_2 + O_3$) are listed in Table S1 in the Supplement.

In a typical experiment, the starting concentrations of O_3 and H_2 were $\approx 5 \times 10^{14}$ and ≈ 5–7×10^{15} molec. cm^{-3}. As described previously (Bunkan et al., 2018), this scheme generates not only OH radicals but also via, for example, Reaction (R3) HO_2. HO_2 is not expected to react with MSAM but will influence the course of secondary reactions in this system (e.g. by reacting with organic peroxy radicals) and thus the end-product distribution, as described in detail in Sect. 3.5. Simulations of the radical concentrations when generating OH in this manner indicate that the HO_2/OH ratio is approximately 30, with individual concentrations of $\approx 1 \times 10^{11}$ molec. cm^{-3} HO_2 and 3×10^9 molec. cm^{-3} OH.

As an OH source, the photolysis of O_3 in the presence of H_2 has the advantage over other photochemical sources (e.g. photolysis of H_2O_2, HONO, or CH_3ONO) that neither H_2 nor O_3 has strong absorption features in the infrared, resulting in a less cluttered spectrum which simplifies retrieval of concentration–time profiles of reactants and products.

2.3 Chemicals

A commercially available sample of methane sulfonamide (Alfa Aesar, > 98 %) was used. O_3 was generated by flowing synthetic air (Westfalen) through a stainless-steel tube that housed a low-pressure Hg lamp (PenRay) emitting at 184.95 nm. Synthetic air (Westfalen, 99.999 %), H_2 (Westfalen, 99.999 %), CO_2 (Westfalen 99.995 %), CO (Westfalen, 99.997 %), SO_2 (Air Liquide, 1 ppmv in air), and HC(O)OH (Sigma Aldrich) were obtained commercially. Anhydrous nitric acid was prepared by mixing KNO_3 (Sigma Aldrich, 99 %) and H_2SO_4 (Roth, 98 %) and condensing HNO_3 vapour into a liquid nitrogen trap.

2.4 Relative rate constant determination

The rate constant (k_4) of the reaction between OH and $CH_3SO_2NH_2$ (Reaction R4) was measured using the relative rate method using (in different experiments) formic

acid (HC(O)OH), acetone ($CH_3C(O)CH_3$), and methanol (CH_3OH) as reference compounds.

$$CH_3S(O)_2NH_2 + OH \rightarrow \text{products} \quad \text{(R4)}$$
$$CH_3C(O)CH_3 + OH \rightarrow \text{products} \quad \text{(R5)}$$
$$HC(O)OH + OH \rightarrow \text{products} \quad \text{(R6)}$$
$$CH_3OH + OH \rightarrow \text{products} \quad \text{(R7)}$$

Relative rate constants were derived by monitoring the depletion of one or more IR features of MSAM relative to those of the reference compounds. The following expression links the depletion factors (e.g. $\ln([MSAM]_0/[MSAM]_t)$) to the relative rate coefficient:

$$\ln\left(\frac{[MSAM]_0}{[MSAM]_t}\right) = \frac{k_4}{k_{ref}} \ln\left(\frac{[ref]_0}{[ref]_t}\right), \quad (1)$$

where $[MSAM]_0$, $[MSAM]_t$, $[ref]_0$, and $[ref]_t$ are the concentrations of MSAM and reference compound at times 0 and t; k_4 and k_{ref} are the rate constants for reactions of OH with the MSAM and reference, respectively. As only relative changes in the IR signal are used in the analysis, absolute concentrations are not required as long as the absorption features used display a linear relation with concentration. Plots of $\ln([MSAM]_0/[MSAM]_t)$ versus $\ln([ref]_0/[ref]_t)$ should therefore be linear, pass through the origin, and have a slope of k_4/k_{ref}. The experimental procedure consisted of filling the cell with a mixture of MSAM/reference/O_3/H_2/N_2 and allowing it to mix (5–10 min) prior to subjecting the mixture to 253.65 nm radiation whilst monitoring IR features at 3–5 min intervals.

This analysis inherently assumes that the only loss process for MSAM and the reference molecules is reaction with OH. Experiments in which the starting gas mixture was allowed to stand for several hours with no discernible loss of MSAM, formic acid, methanol, or acetone confirmed that none of these gases are lost to the wall or react with O_3 to a significant extent. From observation of MSAM and O_3 mixtures, we were able to derive an upper limit for the reaction of MSAM with O_3 of 1×10^{-19} cm^3 molec.$^{-1}$ s^{-1}.

3 Results and discussion

3.1 Vibrational characterization of $CH_3SO_2NH_2$

The experimental, infrared absorption spectrum of MSAM (Fig. 1) shows characteristic bands corresponding to SO_2 stretching vibrations at 1385 and 1172 cm^{-1}, the NH_2 wagging vibration at 857 cm^{-1}, stretching vibrations at 3476 and 3380 cm^{-1}, bending at 1551 cm^{-1}, and the CH_3 wagging band at 976 cm^{-1}. Assignment of the infrared features (Table 1) was made by comparison with a theoretical spectrum calculated using density functional theory (DFT) at the B3LYP/6-311++G(3d,2p) and B3LYP/aug-cc-pVTZ-pp levels of theory for the vibrational characterization of

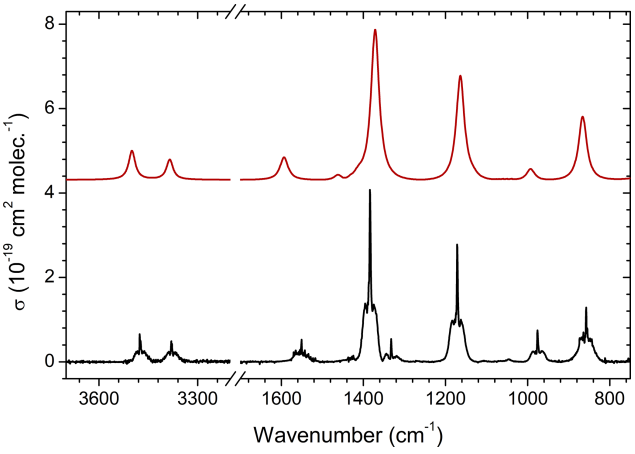

Figure 1. Comparison of the experimental infrared absorption spectrum (black line) of MSAM ($\sim 1 \times 10^{14}$ molec. cm^{-3}) and the calculated spectrum at B3LYP/aug-cc-pVTZ-pp levels of theory (red line). The cross sections (σ) are in base e.

MSAM in the gas phase. These basis sets should be sufficient to describe the relative energies for the isomers. Harmonic vibrational frequencies and zero-point energies (ZPEs) were calculated at these levels of theory to check whether the stationary points obtained were either isomers or first-order transition states (all calculated conformers had only real frequencies). The high-accuracy energy method Gaussian 04 with Møller–Plesset expansion truncated at the second order (G4MP2) was also used for the calculation of the barrier energies. The determination of the Hessian matrix also enabled the calculation of the thermochemical quantities for the conformers at 298.15 K. All symmetry restrictions were turned off in the calculations. All calculations were run with the Gaussian 09 program package (Frisch, 2009). Assuming that the point group for the molecule is Cs, all 24 fundamental modes should be both IR and Raman active, 14 of them belonging to A′ representation and 10 to A″. All the vibrational frequencies are real and positive. The assignments in Table 1 were made from an evaluation of the normal-mode displacement vectors; as many of the modes are strongly coupled, this information is rather subjective. The frequencies of the absorption bands of the theoretical spectrum displayed in Fig. 1 were adjusted by a scaling factor of 0.968 ± 0.019 recommended for the B3LYP/aug-cc-pVTZ level of theory (column "ratio" in Table 1) (Halls et al., 2001).

If the "cold trap" is removed, extra absorption bands originating from the MSAM dimer are observed. These slowly disappear with time as the condensation of the low-volatility dimer to the reactor surfaces takes place. Figure S1 shows the IR spectra of the dimer after the subtraction of the monomer. A complete characterization of the vibrational modes is presented in Table S1. According to our calculations, two hydrogen-bond interactions between the −HNH···OSO- are formed in the dimer which produce a bathochromic shift of

Table 1. Experimental and calculated vibrational wavenumbers for MSAM.

Mode symm.	Mode	Frequencies (cm^{-1})				Mode description
		Experiment[a]	6-31++(d,p)[a,b]	Aug-CC-pVTZ[a,b]	Ratio	
A″	ν_1	3476 (18.8)	3627 (18.8)	3612 (19.6)	0.958	NH_2 asym. stretch
	ν_3		3193 (< 0.1)	3169 (0.2)		CH_3 deformation
	ν_7		1461 (1.1)	1457 (0.4)		CH_3 rocking
	ν_{10}	1383 (100)	1322 (100)	1342 (100)	1.048	SO_2 asym. stretch
	ν_{12}		1085 (2.2)	1087 (1.5)		NH_2 rocking
	ν_{14}		981 (0.3)	972 (0.3)		CH_3 twisting
	ν_{20}		385 (< 0.1)	392 (< 0.1)		C–S–N twist
	ν_{21}		321 (1.1)	328 (1.2)		C–S–N twist
	ν_{23}		218 (0.2)	216 (1.5)		CH_3 twist
	ν_{24}		170(14.9)	179(11.2)		NH_2 twist
A′	ν_2	3380 (17.2)	3512 (13.0)	3508 (13.8)	0.962	NH_2 sym. stretch
	ν_4		3184 (< 0.1)	3161 (< 0.1)		CH_3 asym. stretch
	ν_5		3079 (0.1)	3065 (< 0.1)		CH_3 sym. stretch
	ν_6	1551 (15.6)	1591 (15.2)	1582 (13.5)	0.975	NH_2 bend
	ν_8		1460 (2.5)	1456 (1.9)		CH_3 asym. bend
	ν_9	1428 (3.7)	1363 (3.3)	1350 (4.2)	1.048	CH_3 umbrella
	ν_{11}	1172 (72.8)	1115 (69.6)	1135 (64.2)	1.051	SO_2 sym. stretch
	ν_{13}	976 (17.8)	994 (7.6)	987 (8.9)	0.982	CH_3 wagging
	ν_{15}	857 (43.1)	867 (42.4)	864 (40.8)	0.988	NH_2 wagging
	ν_{16}		704 (7.2)	704 (4.2)		C–S stretch
	ν_{17}		663 (81.9)	649 (81.5)		S–N stretch
	ν_{18}		480 (14.9)	490 (15.8)		SO_2 wagging
	ν_{19}		457 (5.1)	468 (3.5)		SO_2 bend
	ν_{22}		285 (1.8)	290 (1.9)		C–S–N bend

[a] Relative absorbance at band maximum in parentheses. [b] Calculated using the B3LYP method.

the absorption bands. For each kinetic experiment we ensure that no dimer band is present in the initial spectrum.

3.2 Relative rate measurements: determination of k_4

Once the concentrations of MSAM and the reference compound were stable (i.e. mixing in the chamber was complete) the photolysis lamps were switched on for a period of typically 1 h during which FTIR spectra (duration of ∼ 20 s) were obtained every few minutes. The concentrations of the reactants in each individual experiment can be found in Table 2. Figure 2 shows the loss of absorption features due to MSAM and the reference compound (in this case acetone) at different times during the experiment.

The depletion of MSAM was quantified by integrating the Q-branch of the 857, 1172, and 1383 cm^{-1} absorption bands and the complete absorption band at 3380 cm^{-1}. The relative depletion of the MSAM absorption features agreed to within ∼ 5 %. Depletion of the reference gases was quantified by integrating their absorption bands at 1221–1249 cm^{-1} (acetone), 2788–3070 cm^{-1} (methanol), and 1073–1133 cm^{-1} (formic acid). An alternative analysis procedure, in which the relative depletion of MSAM was derived by scaling a reference spectrum of MSAM (e.g. that obtained prior to photoly-

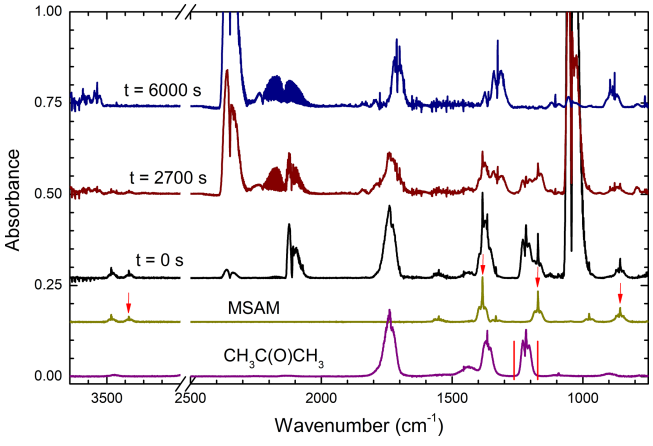

Figure 2. Raw data from a relative rate experiment (using acetone as reference reactant) showing the gradual depletion of reactants and formation of products. The lower two spectra are reference spectra, indicating (red arrows and red min–max lines) which absorption features were used for the relative rate analysis. The strong absorption close to 2100 cm^{-1} at $t = 0$ s is due to O_3. CO_2 and CO absorption bands are centred at ≈ 2350 and 2140 cm^{-1}, respectively.

Table 2. Rate coefficient ratios and experimental conditions for the relative rate experiments.

Reference reactant[a]	Concentration (10^{14} molec. cm^{-3})				Band[e] (cm^{-1})	k_4/k_{ref}	k_4 (10^{-13} cm^3 molec.$^{-1}$ s^{-1})	
	[MSAM][b]	[Ref][c]	[O_3][d]	[H_2][c]				
Acetone	0.31	0.34	7.71	71.8	857	0.792 ± 0.012	1.43 ± 0.10	1.40 ± 0.09[f]
					1172	0.771 ± 0.005	1.39 ± 0.09	
					1383	0.779 ± 0.006	1.40 ± 0.09	
					3380	0.770 ± 0.010	1.39 ± 0.10	
Formic acid	0.56	0.55	5.74	65.2	857	0.312 ± 0.004	1.41 ± 0.11	1.38 ± 0.09[f]
					1172	0.311 ± 0.002	1.40 ± 0.10	
					1383	0.302 ± 0.002	1.36 ± 0.10	
Methanol	0.88	0.25	4.58	46.6	1172	0.159 ± 0.001	1.43 ± 0.17	1.42 ± 0.16[f]
					1383	0.153 ± 0.001	1.38 ± 0.17	
					3380	0.161 ± 0.003	1.45 ± 0.19	

[a] Depletion of reference reactants monitored at 1221–1249, 1073–1133, and 2788–3070 cm^{-1} for acetone, formic acid, and methanol, respectively. [b] Concentration estimated from the absorption cross section reported in Fig. 1. [c] Concentration calculated from the measured pressures. [d] Concentration derived from the absorption cross section of O_3. [e] IR absorption bands of MSAM used for the determination of the concentration change over time. [f] Relative rate constant obtained from the linear fitting of all the data and using $k_4 = (1.8 \pm 0.1) \times 10^{-13}$, $k_5 = (4.5 \pm 0.36) \times 10^{-13}$, and $k_6 = (9.0 \pm 1.3) \times 10^{-13}$ cm^3 molec.$^{-1}$ s^{-1} rate constants (IUPAC, 2019).

sis) to match those at various times after photolysis, was also used. The depletion factors thus obtained were indistinguishable from those using individual absorption features.

Figure 3 shows plots of the depletion factors for MSAM versus those of the three reference compounds following exposure to OH radicals in 700 Torr of synthetic air at 296 K. A linear least-squares analysis of the data gives rate constant ratios $k_4/k_5 = (0.778 \pm 0.008)$, $k_4/k_6 = (0.307 \pm 0.004)$, and $k_4/k_7 = (0.158 \pm 0.002)$ where the quoted errors are 2 standard deviations. Table 2 summarizes the experimental conditions and the rate coefficient ratios obtained when using each MSAM absorption band. The difference between the rate coefficient ratios obtained for the three-absorption-band experiments is always less than 5 %. The rate constant ratios were placed on an absolute basis using evaluated rate coefficients (Atkinson et al., 2006; IUPAC, 2019) whereby $k_5 = (1.8 \pm 0.36) \times 10^{-13}$, $k_6 = (4.5 \pm 1.8) \times 10^{-13}$ and $k_7 = (9.0 \pm 1.8) \times 10^{-13}$ cm^3 molec.$^{-1}$ s^{-1}. We derive values of k_4 (relative to acetone) $= (1.40 \pm 0.28) \times 10^{-13}$, k_4 (relative to formic acid) $= (1.38 \pm 0.55) \times 10^{-13}$, and k_4 (relative to methanol) $= (1.42 \pm 0.28) \times 10^{-13}$ cm^3 molec.$^{-1}$ s^{-1} (where the uncertainties include uncertainty associated with the evaluated rate coefficients for k_5, k_6, and k_7). The values of k_4 obtained using the three different reference compounds are, within experimental uncertainties, identical, indicating the absence of significant systematic errors associated with the use of the reference reactants. We prefer the value of k_4 from the experiment using acetone as reference. For acetone, the relative rate constant is close to unity and the rate coefficient for OH has been extensively studied and is associated with low uncertainty. The preferred value of the rate coefficient, k_4, is $(1.4 \pm 0.3) \times 10^{-13}$ cm^3 molec.$^{-1}$ s^{-1} where the uncertainty is 2σ.

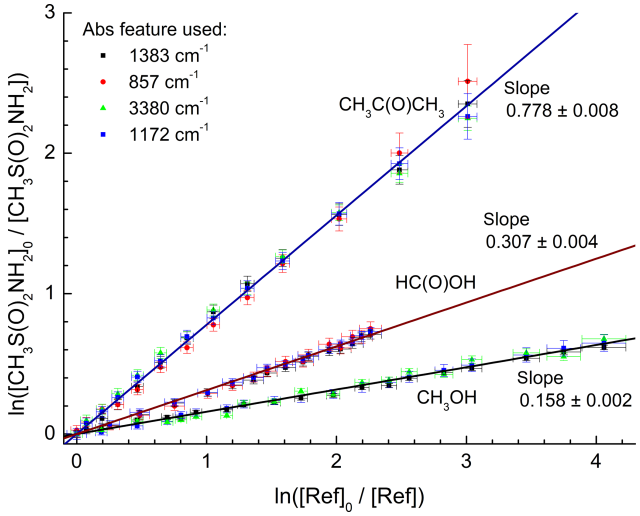

Figure 3. Relative depletion factors for MSAM and the reference compounds $CH_3C(O)CH_3$, HC(O)OH, and CH_3OH obtained at room temperature and a total pressure of 700 Torr of air. The different absorption bands of MSAM used in the analysis are indicated. The slopes are equal to the ratio of rate coefficients k_4/k_{ref} as defined in Eq. (1).

3.3 Product yields

In order to identify and quantify the end products of the title reaction in air, approximately $(6.25 \pm 0.75) \times 10^{13}$ molec. cm^{-3} of MSAM, 4.04×10^{14} molec. cm^{-3} of O_3, and 1.00×10^{15} molec. cm^{-3} of H_2 were loaded into the chamber at a total pressure of 700 Torr of synthetic air and 298 K. Subsequent to initiation of the reaction between OH

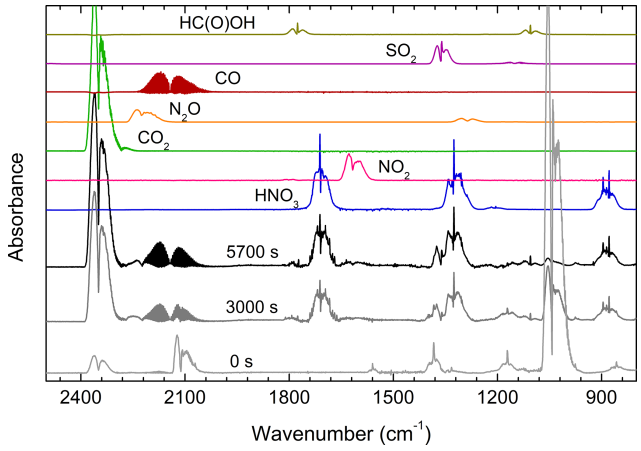

Figure 4. Infrared spectrum acquired prior to (0 s) and after (3000 and 5700 s) photolysis of a mixture of MSAM, O_3, H_2, and air. During irradiation, OH concentrations were $\approx 3\times10^9$ molec. cm^{-3}. H_2O-absorption features have been subtracted from the spectra. Reference spectrum of HNO_3, NO_2, CO_2, N_2O, CO, SO_2, and HC(O)OH recorded under the same experimental conditions (700 Torr and 298 K) are also shown.

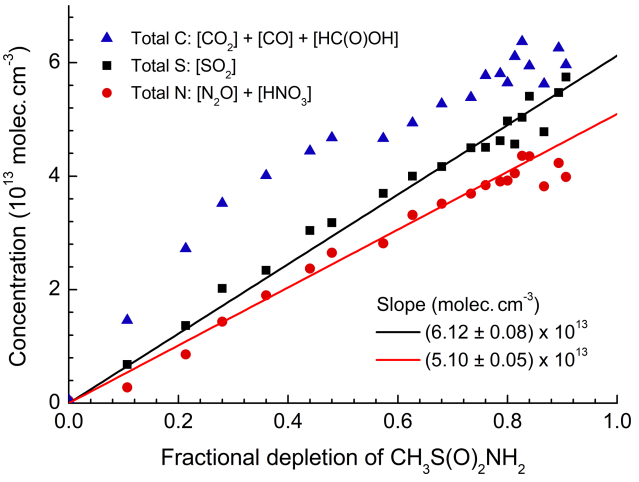

Figure 5. Summed concentration of carbon-containing products (CO_2, CO, and HC(O)OH), sulfur-containing products (SO_2), and nitrogen-containing products (N_2O and HNO_3) plotted versus the relative depletion of MSAM. The slope gives the initial concentration of MSAM assuming stoichiometric conversion to the products listed.

and MSAM by switching the Hg lamps on, IR spectra (700–4000 cm^{-1}) were taken at 300 s intervals.

Figure 4 shows the initial spectrum of the gas mixture with O_3 bands at 903–1068 and 2064–2134 cm^{-1} (A), with the spectrum after 3000 s (B) showing depletion of MSAM and formation of products and the final products after the disappearance of the Q-branches (at 1172 and 1385 cm^{-1}) of MSAM after 5700 s (C). The IR-absorption bands of water vapour have been subtracted from the spectra. Both CO_2 (2387–2300 cm^{-1}) and CO (2226–2050 cm^{-1}) are observed from the photolysis of compounds adsorbed on the walls and surfaces of the cell, and they do not result solely from MSAM degradation.

Figure 4 also displays reference spectra (measured at the same temperature and pressure) of the compounds we identified as reaction products. Other than CO_2 and CO, nitric acid (HNO_3) and sulfur dioxide (SO_2) are easily identified, with weak features from N_2O, NO_2, and formic acid (HC(O)OH) also apparent. The absorption of each product was converted to a concentration using calibration curves that were obtained at the same pressure and temperature (see Fig. S2).

Figure 5 plots the concentration of SO_2 (the only sulfur-containing product observed), the sum of HNO_3+2N_2O (the total reactive nitrogen observed as product), and the sum of CO_2+CO+HC(O)OH (total carbon-containing products observed) versus the fractional depletion of MSAM. The concentrations after 6000 s (when $\sim 90\%$ of the MSAM had reacted) were $[SO_2] = 5.74\times10^{13}$, $[HNO_3] = 3.15\times10^{13}$, $[N_2O] = 4.17\times10^{12}$, $[CO_2] = 4.13\times10^{13}$, $[CO] = 1.65\times10^{13}$, and $[HC(O)OH] = 1.77\times10^{12}$ molec. cm^{-3}. MSAM contains one atom each of sulfur, nitrogen, and carbon. If SO_2, reactive nitrogen, and carbon are conserved, we can derive initial concentrations of MSAM (from the slope) of $6.12\pm0.08\times10^{12}$ molec. cm^{-3} (based on the sulfur balance), $5.10\pm0.05\times10^{12}$ molec. cm^{-3} (based on the nitrogen balance), and $7.4\pm0.2\times10^{12}$ molec. cm^{-3} (based on the carbon balance at the maximum fractional depletion of MSAM). As already mentioned, total carbon is very likely to be overestimated due to its formation and desorption at/from the walls of the chamber. As the main nitrogen product is HNO_3, which has a large affinity for surfaces and which is likely to be lost to the walls, we also expect that use of reactive nitrogen will result in an underestimation of the initial MSAM concentration. For these reasons we believe that the best method to estimate the initial concentration of MSAM is via the formation of SO_2. Figure S3 illustrates the strict proportionality between the relative change of the SO_2 concentration and the MSAM absorption feature at 1384 cm^{-1} in four different experiments. From these four experiments we derive absorption cross sections for MSAM at this wavenumber of $(4.06\pm0.17)\times10^{-19}$ cm^2 molec.$^{-1}$. This value was used to scale the spectrum of MSAM (Fig. 1) and was used to calculate initial concentrations in all other experiments. Figure 6a presents a plot of Δ[product] vs. $-\Delta$[MSAM] from one experiment. Apart from CO, we observe a roughly linear relationship for all products. Time-dependent yields of each product are displayed in Fig. 6b. Whereas the yields of SO_2, CO_2, N_2O, and HC(O)OH are within experimental scatter roughly constant, that of HNO_3 (black line) reaches a constant value only after 800 s, indicating that it is not formed directly, but in a secondary reaction. In contrast, the CO yield is initially slightly larger than unity (indicative of extra sources from the chamber walls) and then decreases with

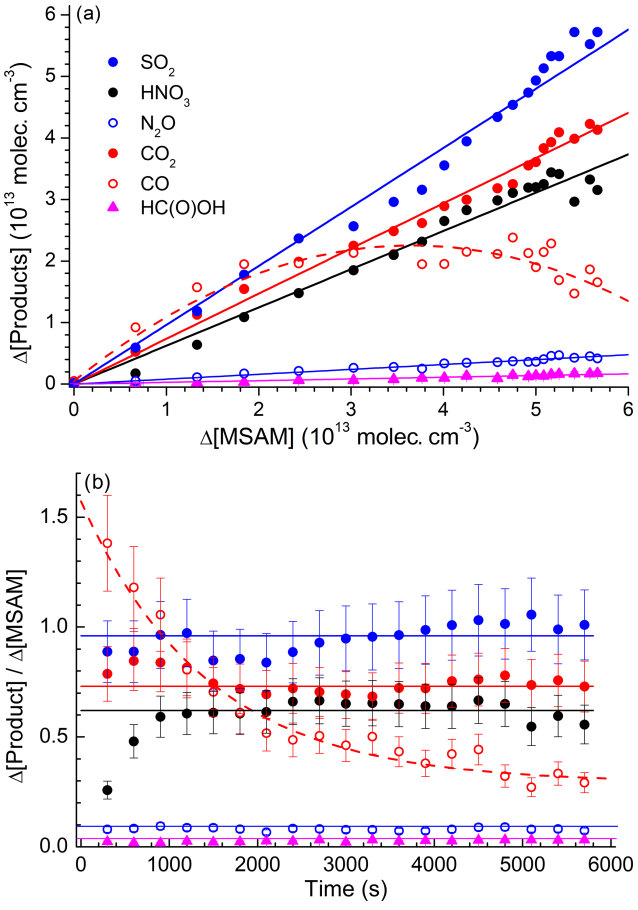

Figure 6. **(a)** Formation of products versus depletion of MSAM. The slopes of the linear fits are the yields of SO_2, HNO_3, CO_2, N_2O, and HC(O)OH from this particular experiment. The polynomial fit to the CO data (red dash line) is added to guide the eye. **(b)** Time dependence of the product yields from the same experiment. The solid, horizontal lines represent the average yield. Error bars are total estimated uncertainty (2σ) including uncertainty in cross sections of products and MSAM.

time as it is removed (via reaction with OH) to form CO_2. The molar yields (after 6000 s of photolysis when MSAM has depleted to $\sim 20\,\%$ of its original concentration) of the products obtained at 298 K and 700 Torr of synthetic air are $\Phi(SO_2) = 0.96 \pm 0.15$, $\Phi(HNO_3) = 0.62 \pm 0.09$, $\Phi(N_2O) = 0.09 \pm 0.02$, $\Phi(CO_2) = 0.73 \pm 0.11$, and $\Phi(HC(O)OH) = 0.03 \pm 0.01$. The slight deviation of $\Phi(SO_2)$ from unity stems from the fact that the quoted yield is at a fixed time, whereas the initial MSAM concentration was derived using all the SO_2 data in this experiment as described above. As N_2O contains two N atoms, the nitrogen balance is thus 0.80 ± 0.13. It is likely that some HNO_3 is lost to reactor surfaces, explaining the deviation from unity. Note that if we had used the nitrogen balance to derive the MSAM IR cross sections, the SO_2 yield would have exceeded unity.

3.4 Reaction mechanism

The time-dependent formation of HNO_3, SO_2, N_2O, and CO provides important clues to the reaction mechanism. Addition to the S atom is not possible so that the initial step will be abstraction of hydrogen by the OH radical, either from the $-CH_3$ group (Reaction R8a) or from the $-NH_2$ group (Reaction R8b).

$$CH_3SO_2NH_2 + OH \rightarrow CH_2SO_2NH_2 + H_2O \quad \text{(R8a)}$$
$$CH_3SO_2NH_2 + OH \rightarrow CH_3SO_2NH + H_2O \quad \text{(R8b)}$$

Based on results of previous studies of the reactions of OH with trace gases containing both CH_3 and $-NH_2$ entities (e.g. CH_3NH_2 or $CH_3C(O)NH_2$), we expect abstraction at the $-CH_3$ group (Reaction R8a) to dominate (Onel et al., 2014; Borduas et al., 2015; Butkovskaya and Setser, 2016). H abstraction at the methyl group is also consistent with a rate coefficient for Reaction (R4) that is very similar to that for OH + acetone.

3.4.1 Abstraction from the $-CH_3$ group

In Sect. 3.4.1 we focus on the fate of the peroxy radical, $OOCH_2SO_2NH_2$, formed by reaction of initially formed $CH_2SO_2NH_2$ with O_2 (Reaction R9). The most important reactions of organic peroxy radicals are self-reactions (Reaction R10) or reactions with NO (Reaction R11), NO_2 (Reaction R12), or HO_2 (Reaction R13).

$$CH_2SO_2NH_2 + O_2 \rightarrow OOCH_2SO_2NH_2 \quad \text{(R9)}$$
$$2\,OOCH_2SO_2NH_2 \rightarrow OCH_2SO_2NH_2 + O_2 \quad \text{(R10)}$$
$$OOCH_2SO_2NH_2 + NO \rightarrow OCH_2SO_2NH_2 + NO_2 \quad \text{(R11)}$$
$$OOCH_2SO_2NH_2 + NO_2 \rightarrow O_2NOOCH_2SO_2NH_2 \quad \text{(R12)}$$
$$OOCH_2SO_2NH_2 + HO_2 \rightarrow HOOCH_2SO_2NH_2 + O_2 \quad \text{(R13)}$$

Peroxy nitrates such as the one formed in Reaction (R12) are thermally unstable with respect to dissociation back to reactants at room temperature, and, given the very low concentrations of NO_2 in our system, Reaction (R12) will not play a significant role in this study.

The oxy-radical $OCH_2SO_2NH_2$ formed in Reactions (R10) and (R11) will react with O_2 to produce an aldehyde (Reaction R14). Alternatively, it could undergo C−S bond cleavage (Reaction R15) to form formaldehyde (CH_2O) and the SO_2NH_2 radical.

$$OCH_2SO_2NH_2 + O_2 \rightarrow HC(O)SO_2NH_2 + HO_2 \quad \text{(R14)}$$
$$OCH_2SO_2NH_2 \rightarrow CH_2O + SO_2NH_2 \quad \text{(R15)}$$

The fate of $HC(O)SO_2NH_2$ will be reaction with OH to form $C(O)SO_2NH_2$ (Reaction R16), which may dissociate to form $CO + SO_2NH_2$ (Reaction R17). The rate coefficient for Reaction (R16) is expected to be $\approx 10^{-11}$ cm^{3}molec.$^{-1}$ s^{-1}

as for many similar reactions of OH with aldehydes (e.g. CH_3CHO).

$$HC(O)SO_2NH_2 + OH \rightarrow C(O)SO_2NH_2 + H_2O \quad (R16)$$

$C(O)SO_2NH_2$ may either decompose to SO_2NH_2 and CO (Reaction R17) or react with O_2 to form an α-carbonyl peroxy radical (Reaction R18).

$$C(O)SO_2NH_2 \rightarrow SO_2NH_2 + CO \quad (R17)$$
$$C(O)SO_2NH_2 + O_2 + M \rightarrow O_2C(O)SO_2NH_2 + M \quad (R18)$$

The fate of $O_2C(O)SO_2NH_2$ is likely to be dominated by reaction with HO_2, which, by analogy to $CH_3C(O)O_2$ (another α-carbonyl peroxy radical), is expected to lead to the reformation of OH (Dillon and Crowley, 2008; Groß et al., 2014).

$$O_2C(O)SO_2NH_2 + HO_2 \rightarrow OH + O_2 + CO_2 + SO_2NH_2 \quad (R19)$$

In both scenarios, SO_2NH_2 is the sulfur-containing product, whereas formation of the peroxy radical in Reaction (R18) will result in early CO_2 formation and OH recycling.

Formaldehyde formed in Reaction (R15) will react with OH to form CO and subsequently CO_2.

$$CH_2O + OH \rightarrow HCO + H_2O \quad (R20)$$
$$HCO + O_2 \rightarrow HO_2 + CO \quad (R21)$$
$$CO + OH(+O_2) \rightarrow CO_2 + HO_2 \quad (R22)$$

But it may also react with HO_2 to form formic acid.

$$CH_2O + HO_2 + M \rightarrow HOCH_2OO + M \quad (R23)$$
$$2HOCH_2OO \rightarrow HOCH_2O + O_2 \quad (R24)$$
$$HOCH_2O + O_2 \rightarrow HC(O)OH + HO_2 \quad (R25)$$

The above reactions explain, at least qualitatively, the observed formation of CO, CO_2, and HC(O)OH. Note that the room temperature rate coefficient for reaction of OH with HCHO is large (8.5×10^{-12} cm^3 molec.$^{-1}$ s^{-1}; Atkinson et al., 2006) compared to that for reaction with CO (2.2×10^{-13} cm^3 molec.$^{-1}$ s^{-1}; Atkinson et al., 2006), which explains why CO was observed as an intermediate product at high concentrations whereas HCHO was not.

The likely fate of the SO_2NH_2 radical formed in Reaction (R15) is either reaction with O_2 to generate SO_2NH or dissociation by S–N bond scission to produce SO_2 and the NH_2 radical.

$$SO_2NH_2 + O_2 \rightarrow SO_2NH + HO_2 \quad (R26)$$
$$SO_2NH_2 \rightarrow SO_2 + NH_2 \quad (R27)$$

We did not observe features in the IR spectrum that could be assigned to SO_2NH based on the spectrum reported by Deng et al. (2016), and we propose that Reaction (R27) is the source of SO_2 as a major reaction product. By analogy with the thermal decomposition of the similar CH_3SO_2 radical, which dissociates to CH_3 and SO_2 on a millisecond timescale (Ray et al., 1996), we expect SO_2NH_2 to decompose stoichiometrically to SO_2 and NH_2 on the timescale of our experiments. The NH_2 radical is known to react with O_3, HO_2, and NO_2 (IUPAC, 2019).

$$NH_2 + O_3 \rightarrow NH_2O + O_2 \quad (R28)$$

$$NH_2 + HO_2 \rightarrow NH_2O + OH \quad (R29a)$$
$$NH_2 + HO_2 \rightarrow HNO + H_2O \quad (R29b)$$

$$NH_2 + NO_2 \rightarrow N_2O + H_2O \quad (R30)$$

NH_2O rearranges within $\sim$ 1 ms to NHOH (Kohlmann and Poppe, 1999), which then reacts with OH or O_2 to generate HNO.

$$NHOH + OH \rightarrow HNO + H_2O \quad (R31)$$
$$NHOH + O_2 \rightarrow HNO + HO_2 \quad (R32)$$

The fate of HNO is the reaction with OH or O_2 to generate NO (Reactions R33 and R34).

$$HNO + O_2 \rightarrow NO + HO_2 \quad (R33)$$
$$HNO + OH \rightarrow NO + H_2O \quad (R34)$$

High concentrations of O_3 ($\approx 10^{14}$ molec. cm^{-3}) and HO_2 ($\approx 10^{11}$ molec. cm^{-3}) in our system ensure that NO is converted to NO_2 in less than 1 s, explaining the non-observation of the IR absorption features of NO.

$$NO + O_3 \rightarrow NO_2 + O_2 \quad (R35)$$
$$NO + HO_2 \rightarrow NO_2 + OH \quad (R36)$$

Finally, NO_2 in this system will react with OH to form the main reactive nitrogen compound we observed, HNO_3.

$$NO_2 + OH + M \rightarrow HNO_3 + M \quad (R37)$$

Thus far we have not considered the reaction of the peroxy radical $OOCH_2SO_2NH_2$ with HO_2 (Reaction R13), which is expected to result in the formation of a peroxide, $HOOCH_2SO_2NH_2$. The most likely fate of $HOOCH_2SO_2NH_2$ is reaction with OH for which (via comparison with CH_3OOH) a rate coefficient close to 1–5 $\times$ 10^{-12} cm^3 molec.$^{-1}$ s^{-1} may be expected with H abstraction from both the peroxide group (Reaction R38) and the adjacent carbon (Reaction R39).

$$HOOCH_2SO_2NH_2 + OH \rightarrow OOCH_2SO_2NH_2 + H_2O \quad (R38)$$
$$HOOCH_2SO_2NH_2 + OH \rightarrow HOOCHSO_2NH_2 + H_2O \quad (R39)$$

Reaction (R38) regenerates the peroxy radical, whereas the $HOOCHSO_2NH_2$ radical may decompose (Reaction R40)

to form formic acid HC(O)OH or decomposes via Reaction (R41) to form the same aldehyde that is generated in Reaction (R14), whilst regenerating OH.

$$HOOCHSO_2NH_2 \rightarrow HC(O)OH + SO_2NH_2 \quad (R40)$$

$$HOOCHSO_2NH_2 \rightarrow OH + HC(O)SO_2NH_2 \quad (R41)$$

The final products are thus the same as those resulting from the self-reaction of the peroxy radical. The path from MSAM to the observed end products including the reactive intermediates that were not observed is illustrated in Fig. 7.

3.4.2 Abstraction from the $-NH_2$ group

In analogy to the reaction between $CH_3C(O)NH_2$ and OH (Barnes et al., 2010), H abstraction from the $-NH_2$ group is expected to result in decomposition of the initially formed CH_3SO_2NH radical via C−S bond fission.

$$CH_3SO_2NH \rightarrow CH_3 + SO_2NH \quad (R42)$$

The methyl radical would react with O_2 to form the methylperoxy radical and in subsequent reactions (via CH_3O) would result in CH_2O formation. As discussed above, CH_2O will be efficiently oxidized to CO and CO_2 in this system. However, the characteristic IR-absorption bands (Deng et al., 2016) of the SO_2NH product were not observed in our experiments, and calculations at the G4MP2 level of theory indicate that Reaction (R42) is endothermic (by 137 kJ mol^{-1}). We conclude that H abstraction from the $-NH_2$ group is a minor channel.

3.5 Kinetic simulation

The proposed reaction mechanism (considering initial reaction by H abstraction from the $-CH_3$ group only) was tested by kinetic simulation using the KINTECUS program package (Ianni, 2015). The reactions used in the chemical scheme and the associated rate coefficients are presented in Table S2. Where experimental rate coefficients were not available, we used rate parameters from similar reactions, and we rationalize these choices in the text associated with Table S2.

Figure 8 shows the variation in the concentrations of the reagent, intermediates, and products observed as a function of time in an experiment conducted at 298 K and 700 Torr of synthetic air. The error bars consider uncertainty associated with the absorption cross sections (5 %–12 %) and uncertainty in deriving the areas of the absorption band areas (less than 3 % in all cases). For MSAM, an uncertainty of ≈ 25 % is expected, based on the indirect method of calibration (see Sect. 3.2). The simulation results are depicted as solid lines.

The good agreement with the N_2O (formed from NH_2 in Reaction R28) and HNO_3 experimental data suggests that the fate of NH_2 (the only source of reactive nitrogen in this system) is accurately described in the model. Note that the wall loss rate of HNO_3 (1×10^{-5} s^{-1}) in the simulation was adjusted to match the HNO_3 profile. The simulated amount of HNO_3 lost to the wall at the end of the experiment was ≈ 14 % of that formed, which helps to explain the non-unity yield of gas-phase nitrogen compounds. The simulations indicate that the maximum concentrations of NO (7×10^9 molec. cm^{-3}) and NO_2 ($\sim 10^{12}$ molec. cm^{-3}) are below the detection limit of the instrument and explain why they were not observed. The strongest absorption features of HCHO (1700–1800 cm^{-1}) overlap with those of H_2O and HNO_3 so that the predicted concentrations of HCHO ($\sim 10^{12}$ molec. cm^{-3}) are also below the detection limit.

The grey line in Fig. 8 represents the sum of $SO_2 + SO_3 + H_2SO_4$, i.e. all model trace gases containing sulfur, which, in the absence of IR absorption features of SO_3 or H_2SO_4, we equate to SO_2. We now draw attention to the fact that SO_2 (the yield of which is constant with time; see Fig. 6) is only well simulated if we neglect its removal by OH (Reaction R43).

$$OH + SO_2 + M \rightarrow HOSO_2 + M \quad (R43)$$

Otherwise, using the preferred rate constant (IUPAC, 2019) at 700 Torr and 298 K of 9.0×10^{-13} cm^3 molec.$^{-1}$ s^{-1} we find that the simulated SO_2 concentration is significantly reduced and its yield is time dependent. At 1 bar of air, collisionally stabilized $HOSO_2$ is converted within 1 µs to HO_2 and SO_3. In the atmosphere, SO_3 reacts with H_2O to form H_2SO_4 (Reaction R45). The conversion of SO_3 to H_2SO_4 may be suppressed under our "dry" conditions.

$$HOSO_2 + O_2 \rightarrow HO_2 + SO_3 \quad (R44)$$

$$SO_3 + (H_2O)_n \rightarrow H_2SO_4 + (H_2O)_{n-1} \quad (R45)$$

SO_2 should therefore not behave like a stable end product in our experiments but be converted to more oxidized forms. In order to confirm that SO_2 is indeed stable in our experiments, we measured the relative rate of loss of SO_2 and acetone under the same experimental conditions (Fig. S4). The apparent relative rate constant k_{43}/k_5 was 0.46, which converts to an effective rate constant for SO_2 loss of 8.2×10^{-14} cm^3 molec.$^{-1}$ s^{-1}. This is more than a factor of 10 lower than the preferred value, indicating that the net rate of the OH-induced SO_2 loss in our system is much lower than expected and not simply governed by the rate constant for the forward reaction to form $HOSO_2$. The reformation of SO_2 under our experimental conditions is the subject of ongoing experiments in this laboratory, which are beyond the scope of the present study. We note that the unexpected behaviour of SO_2 does not significantly impact the conclusions drawn in this work.

The simulation also captures the CO profile well but fails to predict the early formation of CO_2. The match between simulation and experiment could be improved to some extent for CO_2 by amending the fate of the $C(O)SO_2NH_2$ radical as described above (Reactions R17 and R18) so that CO_2 rather

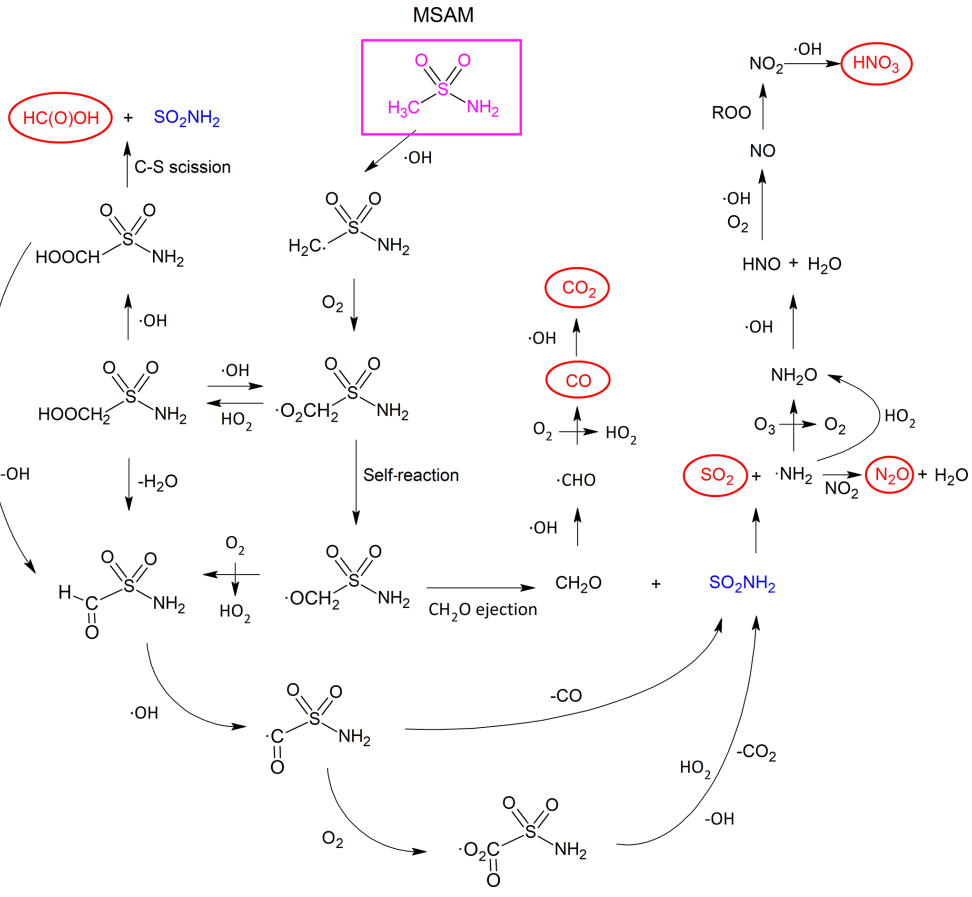

Figure 7. Mechanism for the formation of carbon-containing (HC(O)OH, CO, CO_2), nitrogen-containing (HNO_3 and N_2O), and sulfur-containing (SO_2) end products (in red circles) observed in the OH-initiated photo-oxidation of MSAM.

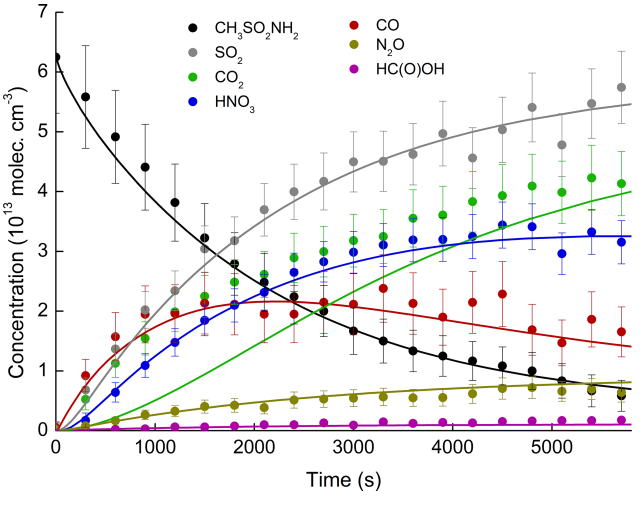

Figure 8. Concentration–time profiles of MSAM and reaction products formed in an experiment at 298 K and 700 Torr air. The error bars represent uncertainty in infrared cross sections. The uncertainty associated with the MSAM concentration is estimated to be $\approx 25\,\%$. Solid lines are simulated profiles.

than CO is formed. The results (Fig. S5) indicate that the improved simulation of CO_2 is accompanied by complete loss of agreement with CO (which is no longer formed in measurable amounts) and poorer agreement with, for example, SO_2 and HNO_3. However, given that CO_2 is generated from the cell walls during irradiation and cannot be used quantitatively (Sect. 3.5), the true fate of the $C(O)SO_2NH_2$ radical remains obscure.

3.6 Atmospheric implications

The rate coefficients for a number of tropospheric, organosulfur trace gases are listed in Table 3. The rate coefficient for the title reaction is significantly lower than those for CH_3SCH_3 (CH_3SCH_3) and $CH_3S(O)CH_3$, (DMSO) for which reaction with OH is the major atmospheric loss process (lifetimes of hours), but it is comparable to $CH_3S(O)_2CH_3$, which also has two S=O double bonds. However, as for most tropospheric trace gases, the lifetime of MSAM will be controlled by a number of processes including photolysis; reactions with the three major oxidants, OH, NO_3, and O_3; and dry deposition (k_{dd}) and heterogeneous uptake to particles (k_{het}), followed by wet deposition.

Table 3. Lifetimes of atmospheric organosulfur trace gases with respect to reaction with OH.

	k(OH)[a]	Lifetime[b]	Reference
$CH_3SO_2NH_2$	1.4×10^{-13}	80 d	This work
$CH_3SO_2CH_3$	$< 3 \times 10^{-13}$	> 40 d	Falbe-Hansen et al. (2000)
$CH_3S(O)CH_3$	5.9×10^{-11}	5 h	Falbe-Hansen et al. (2000)
CH_3SO_2H	9.0×10^{-11}	2.8 h	Burkholder et al. (2015)
CH_3SCH_3	2.2×10^{-12}	1.6 d	Atkinson et al. (2004)

[a] Units of cm^3 molec.$^{-1}$ s^{-1}. [b] Assumes a diel average OH concentration of 1×10^6 molec. cm^{-3}.

The lack of C=C double bonds in MSAM suggest that the reaction with O_3 will be a negligible sink, which is confirmed by the low upper limit to the rate constant of 1×10^{-19} cm^3 molec.$^{-1}$ s^{-1} described in Sect. 2.4. Whereas the reaction with NO_3 represents an important loss mechanism for DMS, we do not expect this to be important for MSAM. CH_3SCH_3 reacts with NO_3 (despite lack of a C=C double bond) as the high electron density around the sulfur atom enables a pre-reaction complex to form prior to H abstraction. This mechanism is not available for MSAM because the electron density around the sulfur atom is reduced by the two oxygen atoms attached to it, which also provide steric hindrance.

Owing to its low vapour pressure, we were unable to measure the UV-absorption spectrum of MSAM, but we note that it was not photolysed at a measurable rate by the 254 nm radiation in our study. We conclude that photolysis in the troposphere, where actinic flux only at wavelengths above ≥ 320 nm is available, is a negligible sink of MSAM.

Therefore, the lifetime of MSAM can be approximated by

$$\tau_{\mathrm{MSAM}} = \frac{1}{k_4\,[\mathrm{OH}] + k_{\mathrm{dd}} + k_{\mathrm{het}}}. \quad (2)$$

Using our overall rate coefficient, $k_4 = 1.4 \times 10^{-13}$ cm^3 molec.$^{-1}$ s^{-1}, for the title reaction and taking a diel-averaged OH concentration of 1×10^6 molec. cm^{-3}, we can use Eq. (2) to calculate a first-order loss rate constant of $k_4[\mathrm{OH}] = 1.4 \times 10^{-7}\,s^{-1}$. Which is equivalent to a lifetime of ≈ 80 d.

MSAM is highly soluble and a dry deposition velocity of $\approx 1\,cm\,s^{-1}$ to the ocean has been estimated (Edtbauer et al., 2019). Combined with a marine boundary height of $\approx 750 \pm 250$ m, this results in a loss rate coefficient of $1.3 \times 10^{-5}\,s^{-1}$ or a lifetime with respect to uptake to the ocean of less than 1 d. Wet deposition is also likely to play a role, which may limit the MSAM lifetime to days under rainy conditions and to weeks in dry regions.

To a first approximation the heterogeneous loss rate of a trace gas to a particle is given by

$$k_{\mathrm{het}} = 0.25\,\gamma \bar{c} A, \quad (3)$$

where γ is the uptake coefficient which represents the net efficiency (on a per collision basis) of transfer of MSAM from the gas phase to the particle phase, $\bar{c}$ is the mean molecular velocity of MSAM ($\sim 26\,000\,cm\,s^{-1}$), and A is the surface area density of particles ($cm^2\,cm^{-3}$) for which a typical value in lightly to moderately polluted regions would be $1 \times 10^{-6}\,cm^2\,cm^{-3}$. A rather low uptake coefficient of $\sim 2 \times 10^{-5}$ would then be sufficient to compete with MSAM loss due to reaction with OH, but a value of 2×10^{-3} would be necessary to compete with dry deposition.

4 Conclusions

The rate coefficient for reaction of methane sulfonamide (MSAM) with OH was determined using the relative rate method as $(1.4 \pm 0.3) \times 10^{-13}$ cm^3 molec.$^{-1}$ s^{-1}. The major, stable, quantifiable sulfur- and nitrogen-containing end products of the reaction are SO_2 and HNO_3 with molar yields of (0.96±0.15) and (0.62±0.09), respectively. CO and CO_2 are the dominant carbon-containing products. N_2O and HC(O)OH were also observed at lower yields of (0.09±0.02) and (0.03±0.01), respectively. The end products (and the low rate coefficient) are consistent with an initial abstraction by OH from the CH_3 group. Based on our results MSAM has an atmospheric lifetime with respect to loss by reaction with OH of about 80 d, indicating that other processes (e.g. deposition) will likely dominate.

Data availability. The rate coefficients measured during this experimental study are listed in Table 2.

Supplement. The supplement related to this article is available online at: https://doi.org/10.5194/acp-20-2695-2020-supplement.

Author contributions. The experiments and data analysis were carried out by MB and DA. The preparation of the paper was performed by MB and JNC, with contributions from DA, JL, JW, and AE.

Competing interests. The authors declare that they have no conflict of interest.

Financial support. The article processing charges for this open-access publication were covered by the Max Planck Society.

Review statement. This paper was edited by James B. Burkholder and reviewed by two anonymous referees.

References

Andreae, M. O.: Ocean-atmosphere interactions in the global biogeochemical sulfur cycle, Mar. Chem., 30, 1–29, https://doi.org/10.1016/0304-4203(90)90059-l, 1990.

Andreae, M. O. and Crutzen, P. J.: Atmospheric aerosols: Biogeochemical sources and role in atmospheric chemistry, Science, 276, 1052–1058, https://doi.org/10.1126/science.276.5315.1052, 1997.

Atkinson, R., Baulch, D. L., Cox, R. A., Crowley, J. N., Hampson, R. F., Hynes, R. G., Jenkin, M. E., Rossi, M. J., and Troe, J.: Evaluated kinetic and photochemical data for atmospheric chemistry: Volume I – gas phase reactions of O_x, HO_x, NO_x and SO_x species, Atmos. Chem. Phys., 4, 1461–1738, https://doi.org/10.5194/acp-4-1461-2004, 2004.

Atkinson, R., Baulch, D. L., Cox, R. A., Crowley, J. N., Hampson, R. F., Hynes, R. G., Jenkin, M. E., Rossi, M. J., Troe, J., and IUPAC Subcommittee: Evaluated kinetic and photochemical data for atmospheric chemistry: Volume II – gas phase reactions of organic species, Atmos. Chem. Phys., 6, 3625–4055, https://doi.org/10.5194/acp-6-3625-2006, 2006.

Barnes, I., Solignac, G., Mellouki, A., and Becker, K. H.: Aspects of the Atmospheric Chemistry of Amides, Chem. Phys. Chem., 11, 3844–3857, https://doi.org/10.1002/cphc.201000374, 2010.

Bates, T. S., Lamb, B. K., Guenther, A., Dignon, J., and Stoiber, R. E.: Sulfur emissions to the atmosphere from natrural sources, J. Atmos. Chem., 14, 315–337, https://doi.org/10.1007/bf00115242, 1992.

Borduas, N., da Silva, G., Murphy, J. G., and Abbatt, J. P. D.: Experimental and Theoretical Understanding of the Gas Phase Oxidation of Atmospheric Amides with OH Radicals: Kinetics, Products, and Mechanisms, J. Phys. Chem. A, 119, 4298–4308, https://doi.org/10.1021/jp503759f, 2015.

Bunkan, A. J. C., Srinivasulu, G., Amedro, D., Vereecken, L., Wallington, T. J., and Crowley, J. N.: Products and Mechanism of the OH initiated photo oxidation of perfluoro ethyl vinyl ether, $C_2F_5OCF{=}CF_2$, Phys. Chem. Chem. Phys., 20, 11306–11316, 2018.

Burkholder, J. B., Sander, S. P., Abbatt, J., Barker, J. R., Huie, R. E., Kolb, C. E., Kurylo, M. J., Orkin, V. L., Wilmouth, D. M., and Wine, P. H.: Chemical Kinetics and Photochemical Data for Use in Atmospheric Studies, Evaluation No. 18, JPL Publication 15–10, Jet Propulsion Laboratory, Pasadena, available at: http://jpldataeval.jpl.nasa.gov (last access: 27 February 2020), 2015.

Butkovskaya, N. I. and Setser, D. W.: Branching Ratios and Vibrational Distributions in Water-Forming Reactions of OH and OD Radicals with Methylamines, J. Phys. Chem. A, 120, 6698–6711, https://doi.org/10.1021/acs.jpca.6b06411, 2016.

Charlson, R. J., Lovelock, J. E., Andreae, M. O., and Warren, S. G.: Oceanic phytpoplankton, atmospheric sulfur, cloud albedo and climate, Nature, 326, 655–661, https://doi.org/10.1038/326655a0, 1987.

Crowley, J. N., Saueressig, G., Bergamaschi, P., Fischer, H., and Harris, G. W.: Carbon kinetic isotope effect in the reaction CH_4 + Cl: a relative rate study using FTIR spectroscopy, Chem. Phys. Lett., 303, 268–274, 1999.

Deng, G. H., Wu, Z., Li, D. Q., Linguerri, R., Francisco, J. S., and Zeng, X. Q.: Simplest N-Sulfonylamine $HNSO_2$, J. Am. Chem. Soc., 138, 11509–11512, https://doi.org/10.1021/jacs.6b07966, 2016.

Dillon, T. J. and Crowley, J. N.: Direct detection of OH formation in the reactions of HO_2 with $CH_3C(O)O_2$ and other substituted peroxy radicals, Atmos. Chem. Phys., 8, 4877–4889, https://doi.org/10.5194/acp-8-4877-2008, 2008.

Edtbauer, A., Stönner, C., Pfannerstill, E. Y., Berasategui, M., Walter, D., Crowley, J. N., Lelieveld, J., and Williams, J.: A new marine biogenic emission: methane sulfonamide (MSAM), DMS and $DMSO_2$ measured in air over the Arabian Sea, Atmos. Chem. Phys. Discuss., https://doi.org/10.5194/acp-2019-1021, in review, 2020.

Falbe-Hansen, H., Sorensen, S., Jensen, N. R., Pedersen, T., and Hjorth, J.: Atmospheric gas-phase reactions of dimethylsulphoxide and dimethylsulphone with OH and NO_3 radicals, Cl atoms and ozone, Atmos. Environ., 34, 1543–1551, 2000.

Frisch, M. J., Trucks, G. W., Schlegel, H. B., Scuseria, G. E., Robb, M. A., Cheeseman, J. R., Scalmani, G., Barone, V., Mennucci, B., Petersson, G. A., Nakatsuji, H., Caricato, M., Li, X., Hratchian, H. P., Izmaylov, A. F., Bloino, J., Zheng, G., Sonnenberg, J. L., Hada, M., Ehara, M., Toyota, K., Fukuda, R., Hasegawa, J., Ishida, M., Nakajima, T., Honda, Y., Kitao, O., Nakai, H., Vreven, T., Montgomery Jr., J. A., J. Peralta, E., Ogliaro, F., Bearpark, M., Heyd, J. J., Brothers, E., Kudin, K. N., Staroverov, V. N., Kobayashi, R., Normand, J., Raghavachari, K., Rendell, A., Burant, J. C., Iyengar, S. S., Tomasi, J., Cossi, M., Rega, N., Millam, J. M., Klene, M., Knox, J. E., Cross, J. B., Bakken, V., Adamo, C., Jaramillo, J., Gomperts, R., Stratmann, R. E., Yazyev, O., Austin, A. J., Cammi, R., Pomelli, C., Ochterski, J. W., Martin, R. L., Morokuma, K., Zakrzewski, V. G., Voth, G. A., Salvador, P., Dannenberg, J. J., Dapprich, S., Daniels, A. D., Farkas, Ö., Foresman, J. B., Ortiz, J. V., Cioslowski, J., and Fox, D. J.: Gaussian 09, Gaussian, Inc., Wallingford CT, 2009.

Groß, C. B. M., Dillon, T. J., Schuster, G., Lelieveld, J., and Crowley, J. N.: Direct kinetic study of OH and O_3 formation in the reaction of $CH_3C(O)O_2$ with HO_2, J. Phys. Chem. A, 118, 974–985, https://doi.org/10.1021/jp412380z, 2014.

Halls, M. D., Velkovski, J., and Schlegel, H. B.: Harmonic frequency scaling factors for Hartree-Fock, S-VWN, B-LYP, B3-LYP, B3-PW91 and MP2 with the Sadlej pVTZ electric property basis set, Theor. Chem. Acc., 105, 413–421, 2001.

Ianni, J. C.: Kintecus v. 5.5, available at: http://www.kintecus.com (last access: 27 February 2020), 2015.

IUPAC: Task Group on Atmospheric Chemical Kinetic Data Evaluation (Ammann, M., Cox, R. A., Crowley, J. N., Herrmann, H., Jenkin, M. E., McNeill, V. F., Mellouki, A., Rossi, M. J., Troe,

J., and Wallington, T. J.), available at: http://iupac.pole-ether.fr/index.html, last access: October 2019.

Kohlmann, J.-P. and Poppe, D.: The tropospheric gas-phase degradation of NH_3 and its impact on the formation of N_2O and NO_x, J. Atmos. Chem., 32, 397–415, 1999.

Onel, L., Blitz, M., Dryden, M., Thonger, L., and Seakins, P.: Branching Ratios in Reactions of OH Radicals with Methylamine, Dimethylamine, and Ethylamine, Environ. Sci. Technol., 48, 9935–9942, https://doi.org/10.1021/es502398r, 2014.

Ray, A., Vassalli, I., Laverdet, G., and LeBras, G.: Kinetics of the thermal decomposition of the CH_3SO_2 radical and its with NO_2 at 1 Torr and 298 K, J. Phys. Chem., 100, 8895–8900, https://doi.org/10.1021/jp9600120, 1996.

Remko, M.: Theoretical study of molecular structure and gas-phase acidity of some biologically active sulfonamides, J. Phys. Chem. A, 107, 720–725, https://doi.org/10.1021/jp026980m, 2003.

Spiro, P. A., Jacob, D. J., and Logan, J. A.: Global inventory of sulfur emissions with 1-degree × 1-degree resolution, J. Geophys. Res.-Atmos., 97, 6023–6036, https://doi.org/10.1029/91jd03139, 1992.